Direct observation of three-dimensional short fatigue crack closure behavior in Ti-6Al-4V alloy using ultra-high-resolution X-ray microtomography

Tubei, Valary
Department of Mechanical Engineering, Kyushu University

Toda, Hiroyuki
Department of Mechanical Engineering, Kyushu University

Ketanond, Worapol
Department of Mechanical Engineering, Kyushu University

Fujihara, Hiro
Department of Mechanical Engineering, Kyushu University

他

出版情報：International Journal of Fatigue. 168, pp.107428-, 2023-03. Elsevier
バージョン：

International Journal of Fatigue 168 (2023) 107428

Contents lists available at ScienceDirect

International Journal of Fatigue

journal homepage: www.elsevier.com/locate/ijfatigue

Direct observation of three-dimensional short fatigue crack closure behavior in Ti-6Al-4V alloy using ultra-high-resolution X-ray microtomography

Valary Tubei [a,*], Hiroyuki Toda [a], Worapol Ketanond [a], Hiro Fujihara [a], Osamu Takakuwa [a], Akihisa Takeuchi [b], Masayuki Uesugi [b]

[a] Department of Mechanical Engineering, Kyushu University, 744 Motooka, Nishi-Ku, Fukuoka 819-0395, Japan
[b] Japan Synchrotron Radiation Research Institute, 1-1-1, Kouto, Sayo-cho, Sayo-gun, Hyogo 679-5198, Japan

ARTICLE INFO

Keywords:
Short fatigue crack
3D crack closure
Titanium alloy
Ultra-high-resolution X-ray tomography
Surrogate-based approach

ABSTRACT

Local 3D short fatigue crack closure behavior was investigated in Ti-6Al-4V alloy using ultra-high-resolution X-ray microtomography (XMT). The results show that the inhomogeneous distribution of plasticity-induced and roughness-induced crack closure is caused by the variation of crack path morphologies. These crack path morphologies exhibited heterogeneous plastic deformation at the crack-tips due to the anisotropic nature of α grains and varying extents of crack tilting and twisting caused by the interaction of the crack front with α/α boundary or α/α + β interface. It was revealed via surrogate-based statistical analysis that the Schmid factor has the strongest effect on crack growth rate.

1. Introduction

Crack closure is widely accepted to predominantly increase the resistance force to fatigue crack growth in metallic materials by reducing the stress range experienced at the crack tip [1]. Hence the crack driving force from Paris-Erdogan law [2] is modified by replacing the stress intensity amplitude, ΔK with the effective stress intensity factor,$\Delta K_{eff} = K_{max} - K_{cl}$. Various crack closure mechanisms have been proposed to explain the near-threshold fatigue crack growth behavior. These include plasticity-induced crack closure (PICC), roughness-induced crack closure (RICC) and oxide-induced crack closure (OICC) [3].

Closure mechanisms have been traditionally investigated based on simple two-dimensional (2D) interpretations of closure phenomenon. From these 2D approaches, valuable insights on the micromechanics of closure such as the effects of crack deflection have been acquired. However, these approaches cannot capture the true nature of a three-dimensional (3D) crack whose complex morphology includes the contribution of mixed-mode I, II, and III displacements. Especially, in short fatigue cracks where the crack is highly crystallographic causing crack plane tilt and twist [4,5] which in turn generates highly complex closure behavior. Accordingly, the elucidation of short crack closure mechanisms with the knowledge of the true nature of 3D fracture morphology can only be achieved using 3D approaches.

3D visualization of cracks and the accompanying crack closure in materials is now possible using state-of-art X-ray tomography offering an accurate and rapid method to investigate the fracture process. Using X-ray microtomography (XMT), Toda *et al.*, [6], evaluated the local mixed-mode crack driving forces along a crack front and the contributions of near-tip contact in aluminium alloy. A complex crack closure behavior caused by a combination of modes II and III displacements was observed which would otherwise not be possible via post-failure analyses or other 2D methods for the determination of crack driving forces such as digital image correlation. The association of crack closure processes with the crystallographically rough fracture surfaces has also been reported in [7,8]. By plotting the relationship between crack opening displacement and mode I stress intensity factor, Limodin *et al.*, [9], showed that non-uniform distribution of crack closure influences the local stress intensity factor which result in inhomogeneity of crack growth rates along the crack front. Ravi *et al.*, [10] confirmed experimentally that the underlying crack closure mechanism for short fatigue cracks is the reversal of stresses at the crack tip. According to these authors, the spatially heterogeneous crack closure is caused by the non-uniform compressive stress distribution which is governed by the stress state of grains in the near-front region.

* Corresponding author.
E-mail address: tubei.valary.059@s.kyushu-u.ac.jp (V. Tubei).

https://doi.org/10.1016/j.ijfatigue.2022.107428
Received 31 August 2022; Received in revised form 31 October 2022; Accepted 21 November 2022
Available online 25 November 2022

Nomenclature

a	Crack depth in thickness direction
CTOD	Crack tip opening displacement
da/dN	Fatigue crack growth per cycle: where, N is the number of cycles
K_{cl}	Crack closure load level
K_I	Mode I stress intensity factor
K_{max}	Stress intensity at maximum load
K_{min}	Stress intensity at minimum load
R	Stress ratio ($=K_{min}/K_{max}$)
PICC	Plasticity induced crack closure
RICC	Roughness induced crack closure
σ_y	Yield stress
ΔK	Stress intensity factor range

The present authors have recently investigated 3D short crack closure behavior in Ti-6Al-4V alloy via synchrotron XMT at a spatial resolution of 1 μm [11]. By separating near-front closure (mainly PICC) and behind-front closure (mainly RICC), the role of crack tilting (mode II) and crack twisting (mode III) in the overall closure behavior in the near-front region was revealed. Such complex 3D fracture behavior in the near-front region could be assessed thanks to the high spatial resolution of 1 μm. However, at the maximum stress intensity factor of $7.1MPa\sqrt{m}$ applied in the previous study [11], the estimated crack tip opening displacement (CTOD) is about 0.33 μm which is much smaller than the spatial resolution of 1 μm. As such, at this spatial resolution level, crack closure in the near-front region would be overestimated. Therefore, in Ti-6Al-4V alloy, a spatial resolution level of 1 μm is not sufficient to accurately assess short crack closure behavior in the near-front region.

Improved spatial resolution of submicron level have been made possible owing to the introduction of high-resolution Fresnel zone plates (FZP) in X-ray microscopy experiments in the hard X-ray region [12]. To investigate materials such as titanium alloy, high-energy X-rays which bears a unique advantage of high penetration into materials [13,14] are required. About a decade ago, available X-ray energy was limited to about 10 keV because of the difficulty to fabricate high aspect ratio FZPs [12]. In 2017, a breakthrough in the FZP technique at SPring-8 was realized by Takeuchi *et al.*, [15] who developed the apodization FZP significantly increasing the X-ray energy available for nano-tomography to 30 keV with the capability of achieving spatial resolution level of up to 0.1 μm. This high-resolution imaging technique provides a unique possibility to accurately characterize short crack closure behavior in the near-front region and assess its mixed-mode (I, II, and III) nature in titanium alloys.

In this study, high-energy imaging-type XMT was employed to assess local 3D crack closure behavior in relation to the underlying microstructure and its influence on crack growth rate in Ti-6Al-4V alloy with a bi-modal microstructure. Ultra-high spatial resolution of 0.15 μm was achieved using this technique which is one order of magnitude higher than previously achieved spatial resolution for crack closure observation [6,7,10,11]. This high spatial resolution enabled detailed monitoring of 3D crack morphology evolution with fatigue cycling (4D observation) and its interaction with the underlying phases i.e., α phase and α + β lamellar. In addition, the actual crack morphology including very fine details such as ridges on the fracture surface and crack closure in near-front region could be accurately assessed. To relate the local crack growth behavior to crystallographic orientations, the underlying microstructure around the crack path was analyzed using electron backscatter diffraction (EBSD) coupled with serial sectioning. Owing to the large and diverse sets of information on the crack morphology and crack closure obtained using the ultra-high-resolution imaging-type XMT and details of the microstructure from EBSD, surrogate-based statistical analysis was performed to apportion the contributions of the various factors (i.e., crack closure, crack tip opening displacement, deflection angle, Schmid factor, and equivalent diameter) to the short crack propagation rate.

2. Material and experimental methods

2.1. Material and sample preparation

Ti-6Al-4V alloy with a chemical composition (in mass%) of Al 5.50 ~ 6.75, V 3.50 ~ 4.50, Fe 0.40, O 0.20, H 0.15, C 0.08, and N 0.05 and Ti balance was investigated in this study. This alloy was hot rolled at 800 °C resulting in a 50% overall thickness reduction from an original thickness of 10 mm. After which, it was tempered up to 900 °C for 96 h and subsequently cooled down to room temperature in the furnace. After the thermomechanical treatment, the volume fractions of hexagonal closed-packed primary α phase and α + β lamellar was roughly 65% and 35%, respectively. The average primary α grain size was about 20 μm and the average α-lath widths in α + β lamellar was approximately 1 μm. The microstructure of this alloy is as shown in Fig. 1. Since dual-phase Ti-6Al-4V alloys are prone to large microtextured regions that strongly influence fatigue crack initiation and growth [16,17], the analysis of the texture of the material is important to understand fatigue behavior. The equiaxed α grains of the Ti-6Al-4V alloy with a bi-modal microstructure employed in this work showed random orientations around the crack path as shown in Fig. S1.

A specimen with a cross-section of 800 μm × 800 μm was machined from the heat-treated material using electron discharge machining (EDM). To remove surface microcracks, the specimen was electrochemically polished using a mixture of 6% perchloric acid, 59% butoxyethanol, and 35% methanol by volume. The final gauge section area was 600 μm × 600 μm. To restrict the crack initiation position and follow the main crack in the specimen during fatigue cycling, a notch of 60 μm in length by 20 μm in depth by 4 μm in width was machined on the gauge section using focused ion beam. In-situ fatigue tests were then performed on the specimen as described in the next section.

2.2. In-situ fatigue tests and crack imaging

2.2.1. Fatigue tests

Load-controlled fatigue tests were performed using a piezoelectric fatigue testing machine applying sinusoidal loading with a load ratio, R = 0.1 at a frequency of 15 Hz. The specimen was subjected to a maximum stress of 622 MPa, corresponding to 70% of the yield stress. To observe crack growth behavior and evolution of the crack morphology with crack extension, fatigue cycling was performed and

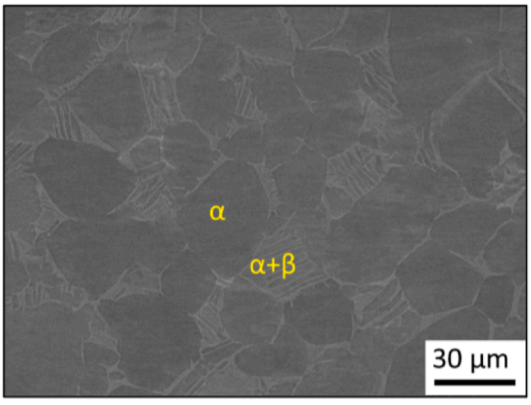

Fig. 1. Microstructure of Ti-6Al-4V alloy after thermomechanical treatment obtained using scanning electron microscope.

stopped intermittently. To eliminate any effects of notch plasticity on the small fatigue crack growth [18], it was ensured that the analyzed crack fronts were outside the notch and the short crack plastic zone region. The applied maximum stress induced a maximum monotonic plastic zone of about 10 μm that was estimated under plane strain conditions by; $r_p = \frac{1}{3\pi}\left(\frac{K_I}{\sigma_y}\right)^2$ [19]. Plane strain condition was confirmed to be predominant for the analyzed specimen with a cross-section of 600 μm by 600 μm since $2.5\left(K_I/\sigma_y\right)^2$ is about 180 μm at the largest crack front which is much smaller than the specimen width. Consequently, the 3D crack morphology and its development through the microstructure with progressive fatigue cycling was visualized at 6 steps. These 6 steps were at 7000, 9400, 11200, 12700, 14200, and 16,300 cycles corresponding to average short crack lengths, a of approximately 43 μm, 48 μm, 54 μm, 56 μm, 70 μm, and 84 μm, respectively. The average crack lengths were determined by averaging the local crack lengths for each 2D slice along the crack front line. The local crack length, a was defined as the distance between the notch and crack tip at a defined angle θ (see the illustration in Fig. S2). The Cartesian coordinates (x, y, z) of the 3D cracks were converted to polar coordinates (r, θ, z) using the approach described in [20]. The 2D slices were then binarized and the crack tip coordinates for each 2D slice were determined. The description of the number of cycles, the corresponding surface crack lengths, and the load levels at which scanning of the crack and crack closure was performed are given in Table 1.

2.2.2. 3D tomographic imaging

High resolution in-situ XMT was performed at BL20XU in SPring-8, Japan to scan the growing crack inside the microstructure and the accompanying crack closure behavior. This in-situ observation of 3D crack growth and closure behavior over time (so-called 4D) was very challenging especially with regards to the design of the mechanical testing rig, the demand for the preparation of a specimen that was small enough to fit the field of view and long scanning time of about 3 days which was laborious and expensive. A monochromatic X-ray beam with photon energy of 30 keV was produced by a liquid nitrogen-cooled Si (1 1 1) double crystal monochromator. A material test rig was set at approximately 80 m from the X-ray source. To characterize the entire 3D crack morphology and accurately examine crack closure in the near-front region in a single specimen, two XMT set-ups were employed namely, projection-type XMT and imaging-type XMT.

(a) Projection-type XMT

Projection-type XMT has the advantage of a large field of view making it possible to scan the entire specimen's gauge section. As such, projection-type XMT was utilized to observe the whole 3D crack shape and crack morphology development with fatigue cycling. In this setup, a 2048 × 2048 pixels CMOS camera was positioned 53 mm behind the sample to capture the projection images (Fig. S3). A spatial resolution of 1 μm was achieved in the reconstructed slices with isotropic voxels of 0.5 μm edges.

Scanning of the specimen's gauge section to observe the 3D crack morphology and crack growth was performed at 80% of the maximum load level corresponding to a load of 165.1 N. Since Ti-6Al-4V alloys are susceptible to creep at room temperature [21], the maximum applied load of 165.1 N was decided after load-drop tests confirmed the absence of cold dwell fatigue during the holding time for scanning of up to 20 min as reported in [11]. Scanning was done at each of the average short crack lengths, a of about 43 μm, 48 μm, 54 μm, 56 μm, 70 μm, and 84 μm, respectively. The details of fatigue tests and scanning load levels are summarized in Table 1. At each step, 3600 scans during 180° stage rotation were captured with exposure time of 50 ms per scan.

(b) Imaging-type XMT

As mentioned, because of the small CTOD below 1 μm in short fatigue cracks in Ti-6Al-V alloy, the characterization of crack closure mechanisms in the near-front region requires high spatial resolution level. Consequently, imaging-type XMT, with the ability to achieve ultra-high spatial resolution was employed to investigate near-front crack closure behavior. In the imaging-type XMT set-up (see Fig. S3), a rotating condenser zone plate that illuminates the specimen was placed between the X-ray source and the sample. An apodization FZP that magnifies the image and a phase plate that generates phase contrast were placed downstream between the specimen and the detector. A second CMOS detector of 2048 × 2048 pixels was placed 165 m behind the specimen in a different experimental hutch. A remarkably high spatial resolution of 0.15 μm measured substantially in the reconstructed images using edge response technique [22,23]. This high spatial resolution enabled the accurate visualization of the crack front, crack morphology, and crack closure in the near-front region. Because the field of view for imaging-type XMT is limited to about ∅60 μm, a local region at the crack front with typical short crack morphology was selected for scanning.

Local observation of crack morphology development with crack extension was undertaken at the near-front region of the cycling steps. Scanning was performed at 80% of the maximum load level. Crack closure observation was performed at the last step corresponding to an average crack length, a of 84 μm. Scanning was performed from 10% to 80% of the maximum load level at intervals of 10% load. For the above observations, 3600 projections scanning 180° were captured to reconstruct a single 3D image at each load level. The exposure time per scan was 100 ms. Following which, the images were volume rendered as described in [11].

Table 1
Fatigue tests and scanning load levels.

Number of cycles	Average crack depth, a	Surface crack length, 2c	Scanning load levels
7000	43 μm	144 μm	80% load
9400	48 μm	159 μm	80% load
11,200	54 μm	169 μm	80% load
12,700	56 μm	175 μm	80% load
14,200	70 μm	197 μm	80% load
16,300	84 μm	215 μm	10–80% load*

*Maximum load: 206.4 N.
*Load increments of 10% up to 80% of the maximum load for crack closure observation at 16,300 cycles

2.3. Microstructure analysis

The underlying microstructure around the crack path was analyzed using EBSD technique coupled with serial sectioning. Here, the fatigued specimen containing a short crack of an average crack length, $a = 84$ μm was mechanically polished through the thickness by serial sectioning to perform EBSD analysis around the crack path. To acquire high quality EBSD data, ion milling was performed on the surface. EBSD analysis was then performed around the crack path at a step size of 0.5 μm to investigate the crystallographic orientations of the grains around the short fatigue crack path. This serial sectioning process was repeated 67 times with a section thickness of 2 μm to obtain the 3D grain shapes.

3. Results

3.1. Global 3D crack morphology and growth variation over time (4D) using projection-type XMT

Fig. 2 shows the extracted 3D crack morphology and its evolution with fatigue cycling analyzed using projection-type XMT. Herein, the underlying Ti-6Al-4V alloy matrix is not displayed. The 3D cracks correspond to the short crack at average crack lengths, a of about 43 μm, 48 μm, 54 μm, 56 μm, 70 μm, and 84 μm in Fig. 2 (a), (b), (c), (d), (e), and (f), respectively. As seen in Fig. 2, the extracted 3D cracks are highly intricate with high fracture surface roughness and consist of overlapped crack segments, deflections, and facet paths. The torturous crack

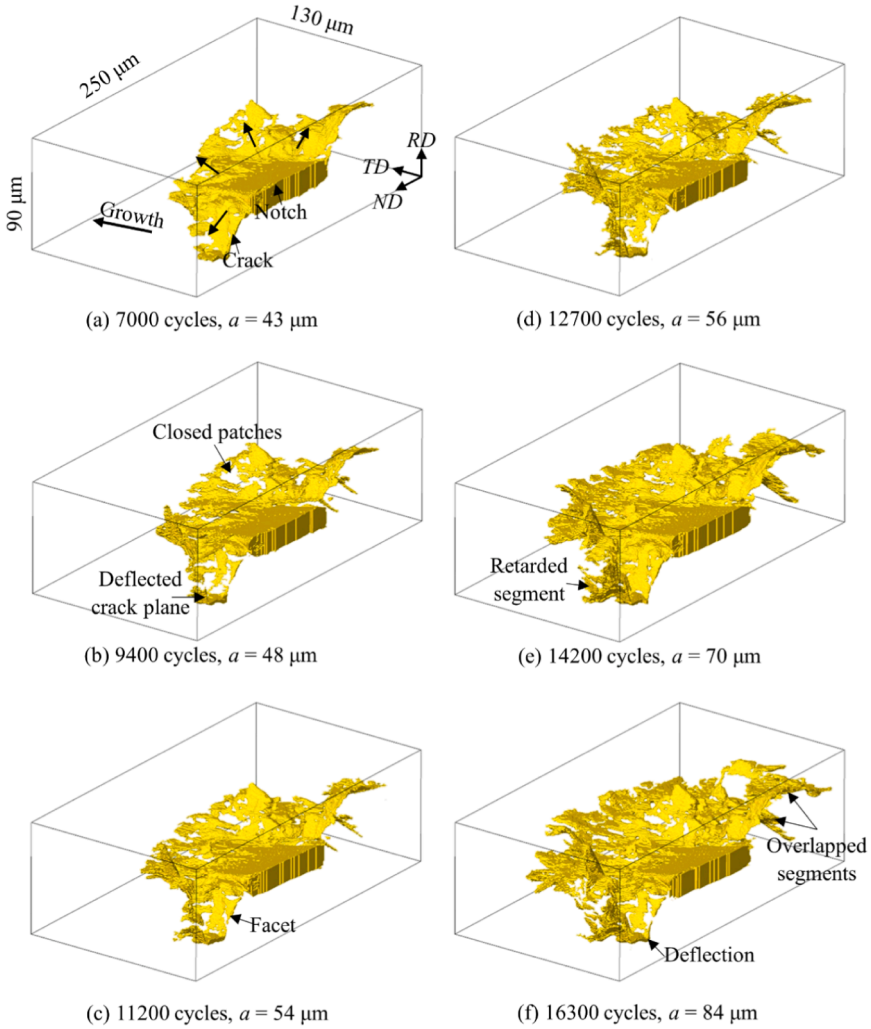

Fig. 2. The complex 3D short fatigue crack morphology consisting of crack deflections, facet paths, and crack branching and its evolution over time (4D) obtained at 80% of the maximum applied load level using projection type XMT at a spatial resolution level of 1 µm. Only the segmented cracks are shown here: the underlying Ti-6Al-4V matrix is not displayed.

morphologies indicate crack growth in mixed-mode I, II, and III despite the specimen being loaded in mode I. In dual-phase Ti-6Al-4V alloy, crack path deviation occurs as the crack front encounters the interface between α grains and α + β lamellar owing to their distinct inherent resistance to crack growth. In addition, due to low restraint on cyclic slip, crack growth along a single slip plane in each grain is promoted in the short crack regime. Therefore, as the crack front approaches α grains with varying crystallographic orientations, crack path deviation occurs due to misorientation between the favorable slip planes [4,20,24] leading to the generation of rough fracture surfaces. Crack path deflection may entail tilting which refers to the inclination of the crack plane with respect to the loading direction where tilt angle is defined as the angle between the intersecting lines of the two favorable slip planes on the cross-section and twisting which is due to out-of-plane shear where the twist angle is defined as the angle between the intersecting lines of the two favorable slip planes on the grain boundary plane [10].

Also, noteworthy Fig. 2 is the non-uniform increase of crack length along the crack fronts with fatigue cycling. This crack growth rate variation along the crack front with fatigue cycling can be clearly visualized from the quantified crack growth rate between the crack fronts as presented in Fig. 3. Note that the crack growth rates in Fig. 3 are plotted against the distance along the crack front measured for the largest crack front at 16,300 cycles. The average crack growth rates for the first three steps i.e., between 7000 and 9400, 9400 and 11,200 and 11,200 and 12,700 cycles are 2.7×10^{-9}, 3.4×10^{-9}, 1.4×10^{-9} m/cycle, respectively as shown by the dashed lines in Fig. 3 (a), (b), and (c). In comparison, in the last two steps corresponding to between 12,700 and 14,200 and 14,200 and 16,300 cycles, the average crack growth rates are 6.9×10^{-9} and 6.4×10^{-9} m/cycle in Fig. 3 (d) and (e), respectively. It is expected that the increase in crack length would result in higher crack growth rates because of the increase in plastic zone size with crack extension. In addition, the inherent resistance of the underlying titanium alloy phases i.e., α phase and α + β lamellar plays a major role in the observed crack growth rate variation. Large portions of the crack fronts in the first 3 steps lie in α + β lamellar which is known to have a high resistance to crack propagation [25] while those of the last two steps lie mostly in α-phase as illustrated in Fig. 3 (f). Moreover, the fracture surface morphology which results from the crack interaction with the underlying microstructure contributes to the heterogeneity of crack growth rate along the crack front. Consider the crack plane to left of the notch in Fig. 2 (b) at 9400 cycles, which was inclined at about 75° with respect to the preceding crack plane. Such pronounced crack plane deviation from the nominal mode I crack growth direction has been reported to reduce the local mode I stress intensity factor experienced at the crack front [26] which possibly slowed the crack growth of this crack segment with fatigue cycling. To understand this complex crack growth behavior, the imaging-type XMT results together with analysis of microstructure will be presented from the next section.

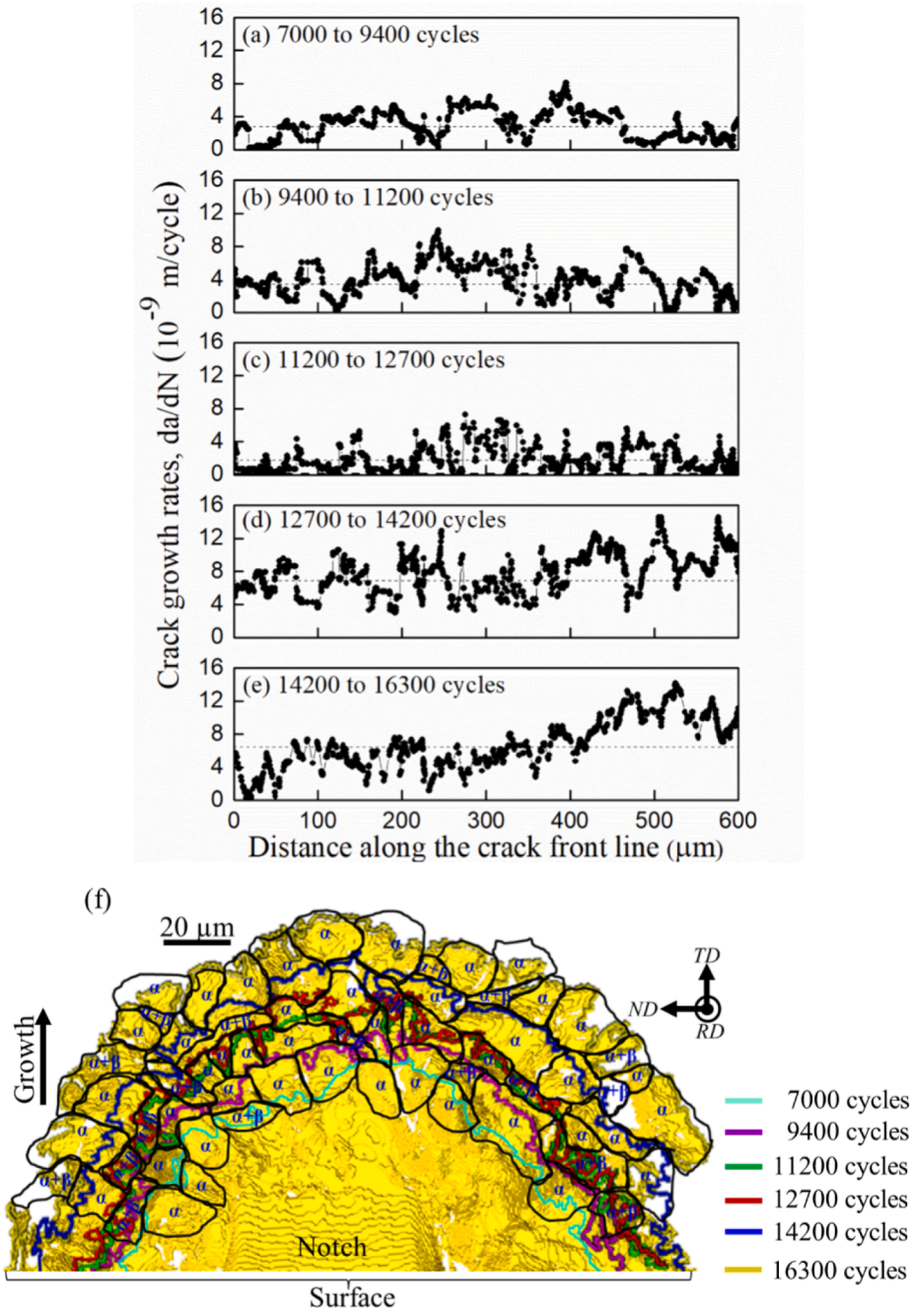

Fig. 3. Crack growth rate variation along the crack front lines and its evolution with fatigue cycling. The crack propagation rates between 7000 and 9400 cycles, 9400 and 11,200 cycles, 11,200 and 12,700 cycles, 12,700 and 14,200 cycles, and 14,200 and 16,300 cycles are presented in (a), (b), (c), (d), and (e), respectively. The dashed lines indicate the average crack growth rate for each of the fatigue intervals. In (f), the α and α + β grains which the crack propagated through are superimposed on the projected crack at 16,300 cycles. The crack fronts of the intermediate fatigue cycles are also shown.

3.2. Assessment of local 3D crack morphology and crack closure using imaging-type XMT

3.2.1. Advantage of imaging-type XMT

Fig. 4 demonstrates the importance of the cutting-edge imaging-type XMT technique. In Fig. 4 (a) a segment of the crack in the near-front region of the crack at the average crack length, *a* of 84 μm is shown. This crack segment was captured using projection-type XMT. The same crack segment captured using imaging-type XMT is presented in Fig. 4 (b). Comparing the crack shapes in Fig. 4 (a) and (b) clearly indicates the limitation of projection-type XMT in determining the true crack front position and visualizing the actual crack morphology. Some segments at the crack front and the regions numbered 1, 2, and 3 were not captured using projection-type XMT which are clearly observed using imaging-type XMT as seen by the highlighted regions in Fig. 4 (a) and (b). As previously mentioned, this is because the crack opening of these crack segments is below the 1 μm spatial resolution attained using projection-type XMT. Therefore, crack closure would be overestimated using projection XMT approach. Evidently, the accurate evaluation of the crack morphology and closure in the near-front region requires ultra-high spatial resolution levels.

3.2.2. Local 3D crack morphology using imaging-type XMT

Fig. 5 shows the local 3D crack morphology of a selected region at the crack front that was followed for the 6 fatigue cycling steps using imaging-type XMT. These crack segments at average crack lengths, *a* of about 43 μm, 48 μm, 54 μm, 56 μm, 70 μm, and 84 μm are presented in Fig. 5 (a), (b), (c), (d), (e), and (f), respectively. These local crack segments were scanned in the near-front region of the cracks that were shown in Fig. 2. An illustration of the field of view of imaging-type XMT

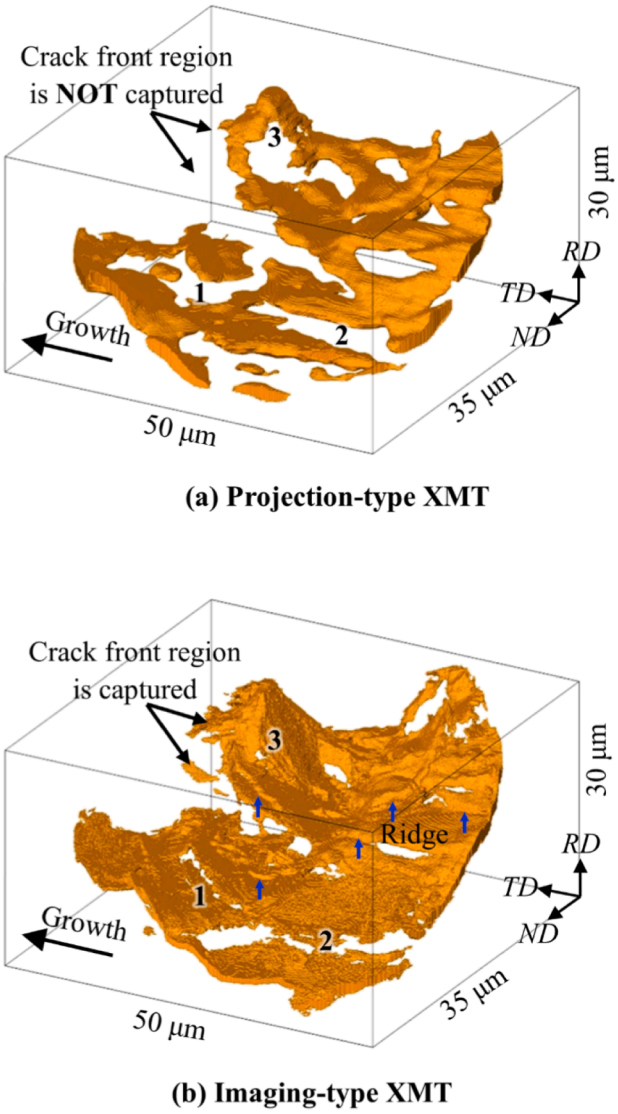

Fig. 4. 3D crack image captured using projection-type XMT at a spatial resolution of 1 µm is shown in (a) and (b) the 3D crack image obtained using imaging-type XMT at a spatial resolution of 0.15 µm showing actual crack front and crack morphology. Both cracks were captured at 80% of maximum load level at an average crack length of $a = 83$ µm corresponding to 16,300 cycles.

on the cracks captured using projection-type XMT is provided in Fig. S4.

The surface topologies and crack front geometry are highly complex even in the near-front region as visualized in Fig. 5. Significant crack plane twist i.e., out-of-plane shear of the crack plane relative to the overall crack growth direction (*TD*-direction) is observed in Fig. 5 (a). This twisted crack plane shows small crack extension with fatigue cycling as observed in Fig. 5 (b), (c), and (d). This indicates that crack propagation resistance is higher in this region than the adjacent crack segments. Crack twist causes a considerably longer fracture path as the crack propagates on a different plane from the preceding crack plane which slows down the crack growth rate [27,28]. After the crack grows out of the twisted crack segment, significant crack extension is observed in Fig. 5 (e) and (f). For an originally advanced crack segment, constraints are exerted by the surrounding uncracked matrix reducing the mode I stress intensity factor [29]. This suggests a redistribution of the crack driving force into the neighbouring locally lagging crack front. The underlying microstructural features and its effects on crack growth rate is presented in the subsequent sections.

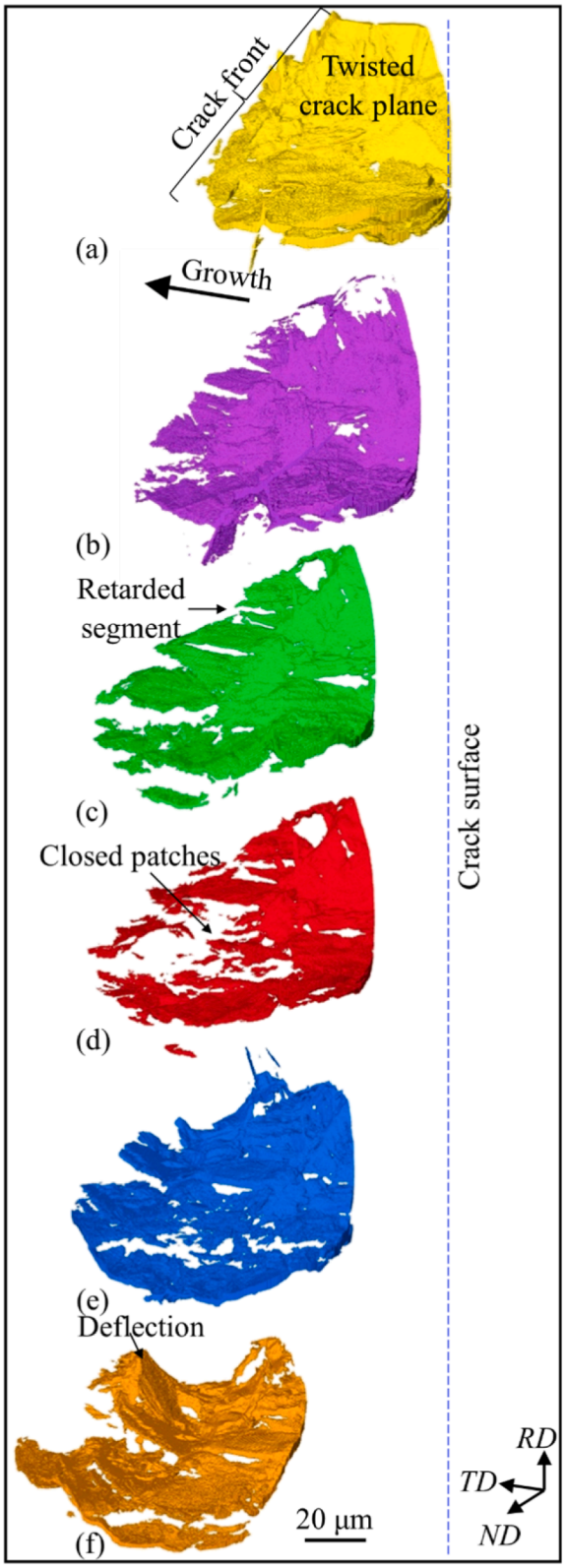

Fig. 5. Local 3D crack growth behavior over time (4D) captured at 80% of the maximum load level using imaging-type XMT technique at a spatial resolution level of 0.15 µm. The crack segment at 7000 cycles ($a = 43$ µm), 9400 cycles ($a = 48$ µm), 11,200 cycles ($a = 54$ µm), 11,200 cycles ($a = 56$ µm), 14,200 cycles ($a = 70$ µm), and 16,300 cycles ($a = 84$ µm) are shown in (a), (b), (c), (d), (e) and (f), respectively.

3.2.3. Local 3D crack growth rates and effects of microstructure

To visualize the crack growth behavior at the near-front region, the crack segments in Fig. 5 were superimposed and the result is presented in Fig. 6 (a). The non-uniform extension of the crack along the crack front with increase in number of cycles is visualized. To understand this complicated crack growth behavior, the underlying microstructure was investigated. In Fig. 6 (b), the α grains along the crack fronts are superimposed on the cracks that were shown in Fig. 6 (a). Herein, the grain color coding corresponds to the EBSD inverse pole figure (IPF) map for the rolling direction (RD) which corresponds to the loading direction. The exposed crack segments between α grains are the regions where the crack grows through α + β lamellar which was not displayed to simplify the figure. A summary of the Schmid factor of the three slip systems i.e., basal, prismatic, and pyramidal in each grain with respect to the macroscopic load and the grain size of the investigated α grains are provided in Table 2.

The local crack propagation rates between the crack fronts as a function of the distance along the crack front is presented in Fig. 7. From this graph, the crack growth rate varies with fatigue cycling and is highly fluctuated along the crack fronts characterized by periods of acceleration and deceleration. This crack growth behavior is strongly linked to the underlying microstructure. As visualized in Fig. 6 (b), the crack grows through three α grains labelled G1, G2, and G3 between 7000 and 9400 cycles. G1 and G2 have larger equivalent diameters of 24.1 μm and 22.6 μm, respectively compared to that of G3 which is 10.7

Table 2
Crystallographic and geometric features of the fractured α grains

Grain ID	Prismatic plane Schmid factor	Basal plane Schmid factor	Pyramidal plane Schmid factor	Equivalent diameter (μm)
G1	**0.46**	0.11	0.44	24.1
G2	0.37	0.34	**0.42**	22.6
G3	0.42	0.21	**0.49**	10.7
G4	**0.49**	0.04	0.45	33.1
G5	**0.49**	0.06	0.46	22.2
G6	0.47	0.20	**0.49**	21.1
G7	0.28	**0.48**	0.31	12.4
G8	**0.49**	0.12	0.47	15.6
G9	**0.49**	0.16	0.48	14.8
G10	**0.43**	0.11	0.41	19.9

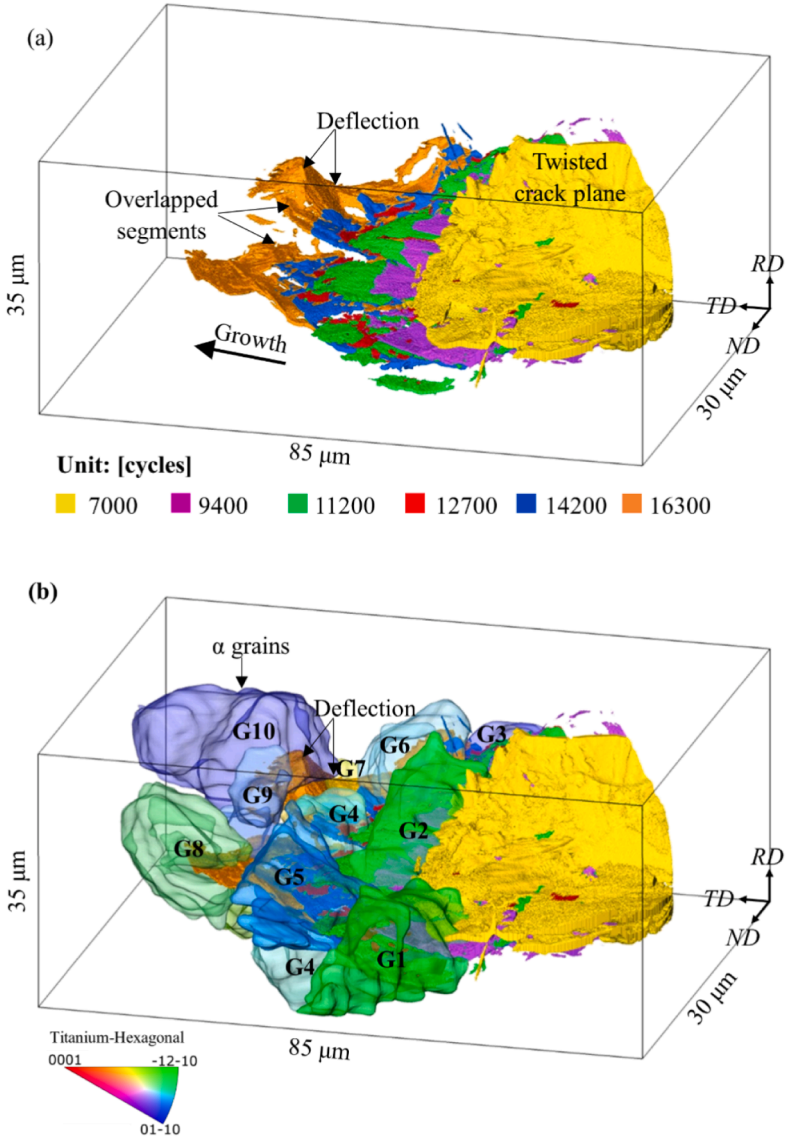

Fig. 6. The superimposed 3D cracks from 7000 cycles (a = 43 μm) to 16,300 cycles (a = 84 μm) captured at 80% of the maximum load using imaging-type XMT technique at a spatial resolution level of 0.15 μm are shown in (a). In (b), the α grains along each crack front are superimposed on the 3D cracks shown in (a). Grain color coding correspond to the IPF map for the rolling direction (RD) which corresponds to the loading direction.

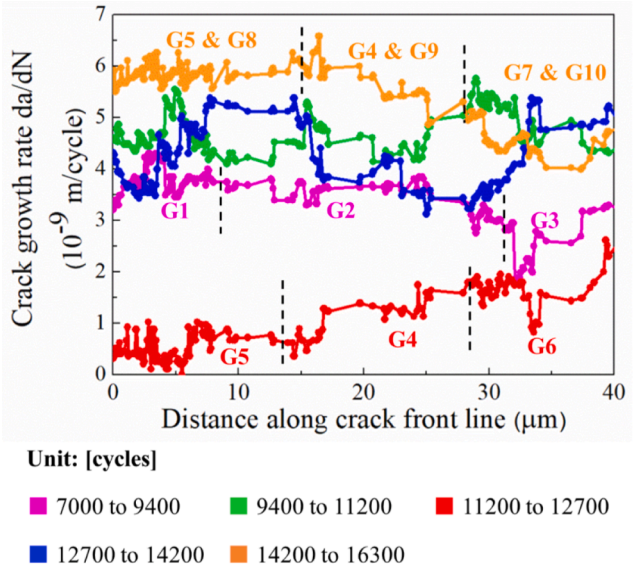

Fig. 7. Crack growth rate variation as a function of the distance along the crack front. The crack growth rates between 7000 and 9400 cycles, 9400 and 11,200 cycles, 11,200 and 12,700 cycles, 12,700 and 14,200 cycles, and 14,200 and 16,300 cycles are presented.

μm. The maximum Schmid factors of G1, G2, and G3 are 0.46, 0.43, and 0.49, respectively. Despite G3 having the highest Schmid factor, crack growth in G3 is lower than in G1 and G2 as seen by the drop of crack growth rate between 7000 and 9400 cycles (pink line) as highlighted in Fig. 7. It is probable that the small grain size of G3 contributed to the observed small crack growth with fatigue cycling. Due to the proximity of the crack front of the crack at 7000 cycles to the grain boundary of G3, it is likely the dislocations emitted at the crack tip were blocked at the grain boundary. This in addition to the highly twisted crack plane behind G3 as shown in Fig. 6 (a) may have contributed to a reduction in the crack driving force slowing down the crack growth.

Notably in Fig. 7 is the crack retardation with fatigue cycling between 11,200 and 12,700 cycles in which the crack growth rates along the crack front were mostly below 2×10^{-9} m/cycle. One reason for this crack retardation is that between G1 and G5 in Fig. 6 (b), part of the crack front grows through $\alpha + \beta$ lamellar which is known to have a high resistance to crack growth [25]. In addition, high misorientation of about 35° was measured between the incoming crack plane in G3 and the outgoing cracked plane in G6. As discussed in [24,30], since short cracks grow along a single plane in each grain, the misorientation between the favorable slip planes of neighboring grains could be the key factor that controls crack growth across the grain boundary. The crack has to change direction as it enters the neighboring grain and in a case where crack plane twist is involved, the wedge of material between the twisted crack planes must be fractured for the crack to pass through the grain boundary offering more resistance to crack growth [5,27]. Note that it has been reported in the same material as the one investigated in the current study that the crack plane can deviate from the favorable plane (plane with high Schmid factor) and grow on an unfavorable slip plane [20]. These authors report that the crack can switch to prismatic slip plane from the preferred basal plane in short crack regime in Ti-6Al-4V when the Schmid factor of the basal plane is low while that of the prismatic plane is high. In addition, the interaction between the 3D crack and grains may induce a low mismatch angle with the neighboring cracked grains causing the crack to switch from one slip system to another as it grows from one grain to the next.

The highest crack growth rates were observed between 14,200 and 16,300 cycles as presented in Fig. 7. After 14,200 cycles, the crack crosses the grain boundaries of G4, G5, and G6 and grows into grows into G7, G8, G9, and G10 with Schmid factors of 0.48, 0.49, 0.48, and 0.43, respectively as seen in Fig. 6 (b) and highlighted in Fig. 7. It seems that this high Schmid factors especially in G7, G8, and G9 may be one factor that contributed to the ease of crack growth through these grains. However, note that the crack propagation rate is not uniform along the crack front: crack growth rate can be seen to decrease from about 28–40 μm along the crack front in Fig. 7 (orange line). For this crack segment, cracked plane in G10 is inclined at about 45° to the preceding cracked plane in G7. This coupled with the local deflection inside G10 as highlighted in Fig. 6 (b) could be the probable cause for the low crack growth rate. On the other hand, in G8 and G9, crack growth occurred primarily in almost straight paths with high alignment between the incoming crack planes and the outgoing crack planes. This may have contributed to the high crack growth rates between 0 and 28 μm along the crack front. The above result is consistent with the report by [20] in their analysis of 3D short crack interaction with the underlying microstructure of Ti-6Al-4V alloy in which high crack growth rate in straight paths compared to zig-zag paths was reported. In addition to the microstructural features and crack morphology, the local stress field is altered by crack closure.

3.2.4. *Local 3D crack closure behavior*

The local 3D crack closure behavior was observed at the average short crack length, *a* of 84 μm which corresponds to 16,300 fatigue cycles. The open cracks (orange color) at 80%, 70%, 60%, 50%, 40%, 30%, 20%, and 10% of the applied load level are shown in Fig. 8. The loss of crack surface with load decrease represents the closed segments (white regions). An example of closed crack segment is highlighted on the 3D crack that was captured at 60% of the maximum applied load level in Fig. 8 (c).

With load decrease, heterogenous spatial distribution of closed patches is observed in Fig. 8. Some crack segments near the crack front remain open even at the minimum load level of 10% as shown in Fig. 8 (h). This closure behavior is strongly associated with the tortuosity of the crack. Crack planes that are highly inclined to the overall crack growth direction show early contact at the point of deflection (see Fig. S5). The sharp crack plane deflection resulted from the change in crack path direction at the grain boundary of neighboring α grains with high misorientation angle as seen in Fig. 6. This suggests that high misorientation angle between adjacent α grains plays a significant role in the generation of RICC.

A significant increase in closed patches was observed as the load was decreased from 60% to 40% load level as seen in Fig. 8 (c), (d), and (e). After which, the closed patches slightly increased with load decrease from 30% to 10% load as seen in Fig. 8 (f), (g), and (h). Therefore, it can be inferred that the macroscopic crack closure load level lies between 60% and 40% load levels. This crack closure is quantified as fractional area of closed patches against the load level in Fig. 9. Due to the distribution of the load steps at which closure was observed, from the plot of fractional area of closed patches against the applied load level in Fig. 9, the closure load level is not definite but can be estimated to be about 40% of the maximum applied load level i.e., the start of non-linearity of fractional area of closed patches. As described in [31], crack closure level can be detected definitely utilizing the unloading elastic compliance method. This compliance technique was applied to estimate the closure load level utilizing the 3D data obtained using imaging-type XMT and compared with the result obtained from fractional area of closed patches plot. Note that the result of the compliance is obtained from the plot of load vs CTOD which is analogous to response obtained using near-tip strain gauge. From the result presented in Fig. 9, the crack closure load level is 57% of the maximum load level at compliance offset of about 2% [31]. Note that the compliance result is strongly associated with PICC since CTOD is measured in the near-tip region. Therefore, the contributions of localized phenomenon far from the crack front such as variation of fracture surface roughness and the associated RICC is not included. Conversely, the plot of fractional area of

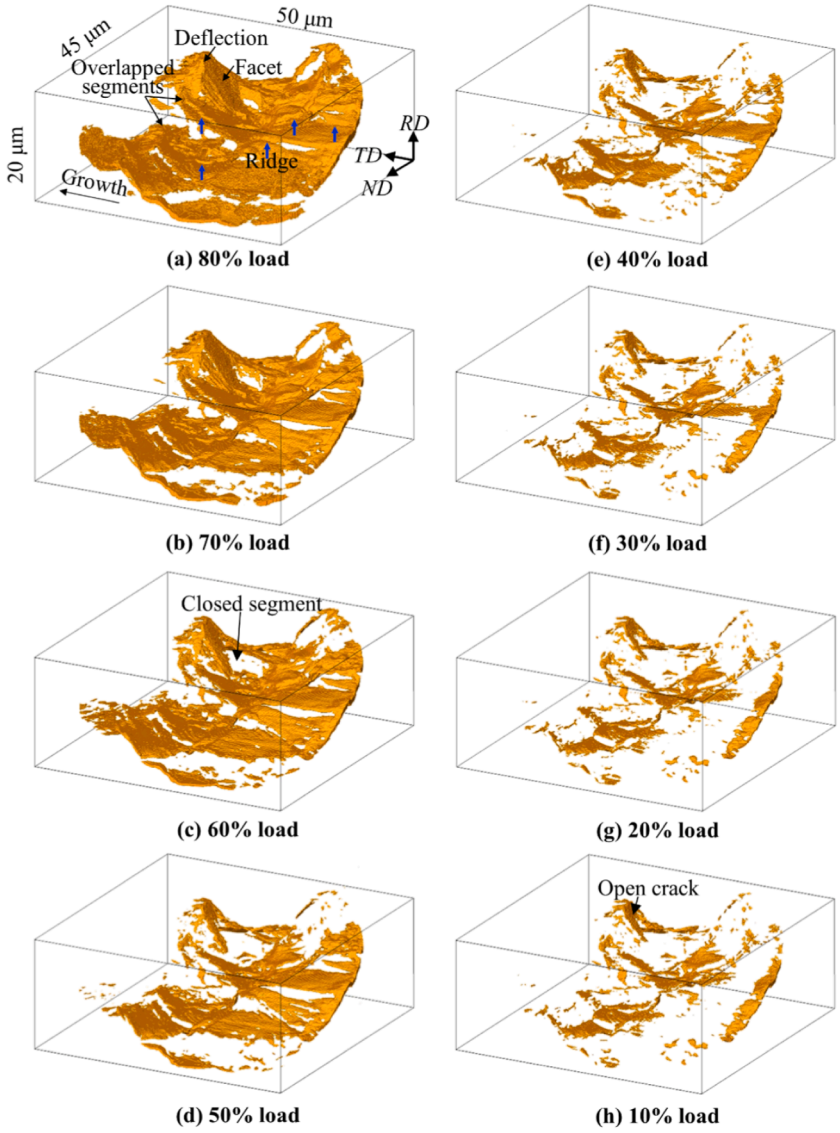

Fig. 8. Local 3D crack morphology and spatial distribution of closed patches captured at an average crack length, $a = 84$ µm corresponding to 16,300 cycles. The crack closure behavior is observed with load decrease from 80% load level shown in (a) to 10% load level in (h). These images were obtained using imaging-type XMT technique at 0.15 µm spatial resolution level.

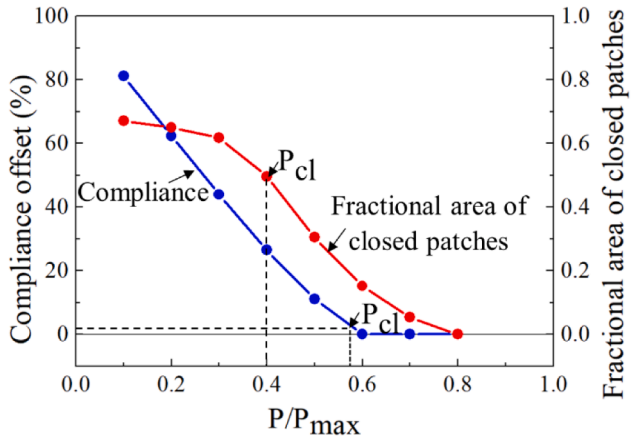

Fig. 9. Estimated closure load level from fractional area of closed patches (PICC + RICC) with load decrease compared to that obtained using compliance method utilizing the 3D crack closure data.

closed patches estimates the actual 3D crack closure behavior by capturing the closure behavior both in the vicinity of the crack front and away from the crack front.

To understand local crack closure behavior, RICC and PICC were separated and analyzed individually. Note that since $2.5(K_I/\sigma_y)^2$ is about 180 µm at the largest crack front i.e., average crack length $a = 84$ µm, plane strain condition is expected to be predominant for the analyzed specimen with a cross-section of 600 µm by 600 µm. Therefore, the cyclic plastic zone (CPZ) which undergoes compressive yielding at the minimum load was estimated under plane strain conditions given by; $r_p = \frac{1}{3\pi}\left(\frac{K_I}{2\sigma_y}\right)^2$ [19]. Note that the CPZ is dependent on the crystallographic orientations of the grains. This is because the measured CPZ ranged between approximately 1.5–3 µm along the crack front which is much smaller than the α grain size of about 20 µm. Therefore, the CPZ will vary grain by grain depending on their orientation with respect to the loading direction [32,33]. It is also worth mentioning that the calculated CPZ from the above equation assumes a circular-shaped CPZ which introduces some inaccuracies since the real plastic zone shape is elongated in the loading direction. In this study, the closed patches

within the CPZ were assumed as mainly due to PICC and those in the remaining crack segment outside the CPZ as mainly RICC. This separation of RICC and PICC is illustrated in Fig. 10 (a) where the region between the blue dashed line and the crack front represents the CPZ. Here, the crack that was captured at 50% load level which was previously presented in Fig. 8 (d) has been superimposed with the crack front line of the crack at 80% load level and projected onto *ND-TD* plane. In Fig. 10 (a), both near-front contact in the CPZ (mainly PICC) and contact away from the vicinity of the crack front (RICC) are observed.

The fractional area of closed patches within the CPZ (mainly PICC) and in the region outside the CPZ (RICC) at 50%, 30% and 10% load levels are shown in Fig. 10 (b) and (c), respectively. Herein, the fractional area of closed patches was defined as the ratio of the closed patches at each load level to the total open crack area of the analyzed region at the maximum applied load of 80%. A fractional area of closed patches of 0 means that the crack is fully open while 1 indicates complete closure.

A general trend of increase in fractional area with load decrease for both PICC and RICC is observed in Fig. 10 (b) and (c). One important observation is the complete contact within the CPZ in some sections along the crack front (between 10 μm and 25 μm) at 50% load level while some sections are not fully closed even at the minimum load of 10% (i.e., between 25 μm and 35 μm) as seen in Fig. 10 (b). This implies that locally, the complete contact of fracture surfaces occurs at different load levels along the crack front. Therefore, heterogeneous crack-tip shielding would be realized along the crack front. From 3D observations, the inhomogeneous distribution of RICC seen in Fig. 10 (a) and (c) can be directly linked to the varying extent of fracture surface roughness i.e., crack tilting and twisting and presence of ridges on the fracture surface due to crack front interaction with local microstructure as previously described in Fig. 8. For example, the high misorientation angle of about 50° measured between G7 and G10 in Fig. 6 (b) caused a large crack deflection angle of about 46° at the grain boundary resulting in early contact at the sharply deflected point as indicated in Fig. 8 (c). As such, the three-dimensional assessment of crack closure using 3D techniques such as X-ray tomography provides a means to evaluate both the mechanisms that control crack closure locally and the determination the macroscopic crack closure level as presented in Fig. 9.

3.2.5. *Effect of crack closure on crack growth rate*

In order to examine the influence of crack closure on crack propagation behavior, the local deformation behavior at the propagating crack front was investigated. The crack driving force in mode I was directly measured from the 3D data in form of local crack tip opening displacement (CTOD). The relationship between the crack deflection angle, RICC, PICC, and CTOD on crack growth rate is presented in Fig. 11.

The measured crack deflection angle is fluctuated along the crack front ranging from 32 to 69°which is expected given the variation of the fracture surface roughness observed in Fig. 8 (a). Here, the deflection angle is defined as the inclination between the previous and the current crack front. Note that the presented crack deflection angle in Fig. 11 is only for the small region investigated using imaging-type XMT and the whole crack front for this crack segment was inclined with respect to the

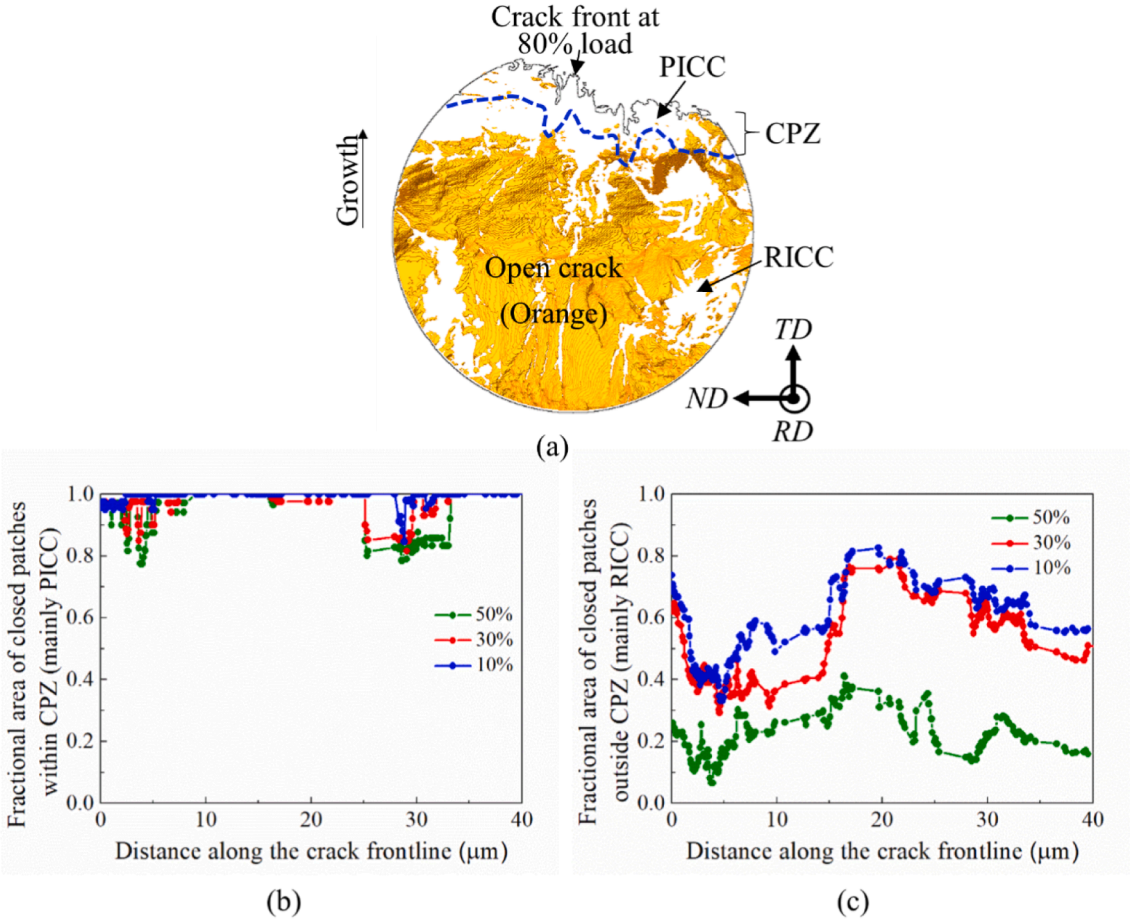

Fig. 10. Separation of RICC and PICC: (a) 3D crack captured at 50% of the maximum load level projected on ND-TD plane showing the analysis of PICC within the cyclic plastic zone (CPZ) and RICC outside the plastic zone area. The fractional area of closed patches within the cyclic plastic zone area (PICC) and outside the plastic zone area (RICC) is presented (b) and (c), respectively.

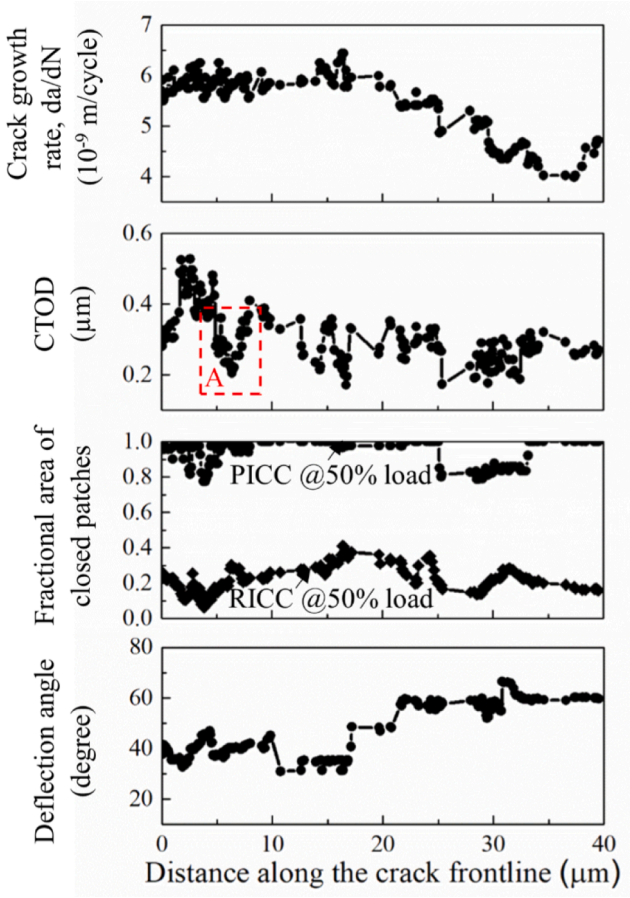

Fig. 11. The complicated crack growth rate caused by the influence of several interacting factors including crack deflection angle, roughness-induced and plasticity-induced crack closure and crack tip opening displacement (CTOD). The deflection angle, fractional area of closed patches, and CTOD were analyzed at the average crack length of $a = 84$ μm corresponding to 16,300 cycles while crack growth rate was analyzed between the crack fronts at 14,200 and 16,300 cycles.

previous crack front. Also from Fig. 11, CTOD fluctuates along the crack front ranging from about 0.17 μm to 0.53 μm which suggests a variation in the extent of local deformation. This can be associated with the heterogeneous inherent resistance of the underlying grains to deformation and crack closure variation which affects the minimum CTOD. There is a general trend of decrease in crack growth rate with decrease in CTOD. However, note that locally, some locations with low CTOD such as the location marked A with CTOD of up to 0.2 μm, does not directly translate to reduced crack propagation rate. This can be attributed to the effects of the adjacent crack segments to the left and right of the section marked A with relatively higher CTOD of more than 0.4 μm. Therefore, because of the 3D effect, it difficult to interpret the effects of the different factors such as crack closure and CTOD on crack growth rate for each point along the crack front.

4. Discussion

4.1. Surrogate-based statistical analysis

The experimental evidence presented above demonstrates the importance of ultra-high spatial resolution to accurately assess near-front crack morphology and the accompanying crack closure behavior. Even though a general view of the effects of the different interacting factors on crack propagation rate is acquired from Fig. 11, it is not clear to what extent each of these competing factors contribute to the observed crack growth rate variation. To solve this issue, statistical methods that can extract common trends and patterns from such large and complex datasets are invaluable. Statistical analysis is particularly indispensable for the characterization of mechanical properties of materials which are heavily dependent on microstructure. But, because of the variability of microstructural patterns in specimens prepared from the same material, many fatigue tests or tensile tests must be performed to reliably describe the mechanical properties of a single material. One statistical method that can effectively address this issue is surrogate-based statistical approach [34] which employs surrogate models to approximate the relationship between multiple input variables (design parameters) and the output (objective function) using a limited number of high-fidelity data such those obtained using X-ray tomography. By leveraging surrogate-based methods, complex engineering design optimization problems such as predicting material properties via the identification of microstructures that lead to certain desired mechanical properties [35,36,37] has been explored in recent years. The application of surrogate-based statistical analysis in the current study is possible owing to the large and diverse sets of information on crack morphology and crack closure obtained using the ultra-high-resolution XMT and details of the microstructure obtained via EBSD coupled with serial sectioning.

To apply surrogate-based statistical analysis, various processing steps are undertaken. In the present analysis, one objective function (crack propagation rate) and six design parameters i.e., crack deflection angle, PICC, RICC, CTOD, Schmid factor, and equivalent diameter of the fractured α grains were prepared to describe the crack and the microstructural features. The distributions and units for each parameter were as follows; crack deflection angle ranged from 32 to 69°, PICC was between 0.1 and 0.7, RICC 0.1 to 0.42, CTOD 0.17 to 0.52 μm, Schmid factor 0.43 to 0.49, equivalent diameter 10.7 to 33.1 μm, and crack growth rate 3.9×10^{-9} to 6.4×10^{-9} m/cycle. Since all these factors have varying ranges and units, the data for all parameters were normalized to range between 0 and 1. Principal component analysis (PCA) [38] was employed to check for multicollinearity between the input variables which occurs when two or more independent variables within the dataset are highly correlated consequently undermining the statistical significance of an independent variable. None of the six design parameters were found to have high correlation based on a predetermined threshold angle (i.e., less than 5°) between the eigenvectors of these variables on the plot of the first and second principal component analysis. After which, global sensitivity analysis [39] which evaluates how the uncertainty in the output can be apportioned to the uncertainties in the input variables was employed to rank the contributions of the above design parameters based on their Pearson correlation coefficient (PCC) [40] with crack growth rate. The values of PCC range between -1 to $+1$ where a value of -1 or $+1$ indicates complete correlation while 0 indicates no correlation between the measured variables. Due to the relatively small data sets (i.e., 195 data points in this study), support vector machine which is a surrogate modelling technique that can effectively handle high-dimensional data [41] was employed. To visualize the multi-dimensional output from surrogate model, response surface methodology [42] was used to explore the relationship between the objective function and design parameters. The above methodology for surrogate-based optimization is described in detail in [43].

4.2. Relationships between various factors that influence short fatigue crack propagation rate

Fig. 12 shows the PCC for Schmid factor, equivalent diameter, deflection angle, CTOD, RICC, and PICC with crack growth rate. The correlation values of these factors with crack growth rate are 0.84, 0.64, 0.41, 0.40, 0.38, and 0.23, respectively. The most contributing input variable to crack growth rate appears to be the Schmid factor with a correlation value of 0.84. It is important to note that the weak

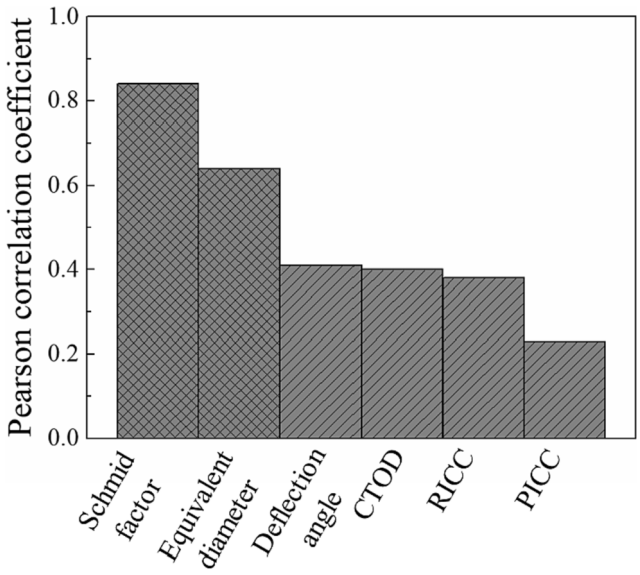

Fig. 12. Correlation between maximum Schmid factor, equivalent diameter, crack deflection angle, crack tip opening displacement (CTOD), roughness induced crack closure (RICC), and plasticity induced crack closure (PICC) with crack propagation rate.

correlation between PICC and RICC with the crack growth rate (Fig. 12) does not imply that closure has less influence on crack propagation rate. In fact, below 50% of the applied load level, PICC and RICC occur without exception along the crack front as observed in Fig. 10 which shields the crack front from the full range of the applied stress. The weak dependency is because the closure load levels associated with PICC and RICC occur almost evenly and at the same time on the investigated crack segment and hence the effects on crack growth rate is not highly varied. Also, since this analysis was limited to small crack segment with a distance of about 0.8 μm between individual slices, it is expected that the crack growth rate of adjacent crack segments would be influenced by the crack closure of neighboring segments. Based on the above discussion, all the design parameters were considered in the surrogate-based statistical analysis.

The rough estimate of the multi-dimensional result of the surrogate-based statistical analysis i.e., 7D (six input variables and one objective function) is summarized using 3D response surface curves which can be interpreted by the human mind as shown in Fig. 13 and Fig. S6. At a glance, it is easy to visualize the optimum and the weakest features from these response surface curves. Only the representative and most effective variables which are shown in Fig. 13 will be discussed. Herein, the 3D response surface curves that explore the relationship between equivalent diameter and Schmid factor, RICC and Schmid factor, PICC and Schmid factor, and deflection angle and CTOD with the crack propagation rate and their 2D projections are shown in Fig. 13 (a), (b), c), and (d), respectively. In Fig. 13 (a) the relationship between the Schmid factor and the equivalent diameter which showed the highest correlation values with crack propagation rate (Fig. 12) is shown. Note that in Fig. 13 (a), the many points with repetitive normalized equivalent diameter and Schmid factor values are because several slices are contained within a single grain. The optimum point occurs when the equivalent diameter is small, and the Schmid factor is low while the weakest point is at large equivalent diameter and high Schmid factor. It is well known that fine grains leads to an increase in grain boundaries which act as barriers to dislocations impeding crack growth [44,45]. Short fatigue crack growth in stage I regime is driven by slip and hence the maximum Schmid factor may be used to represent the crack driving force. It is interesting to note that the weakest point did not correspond to the maximum Schmid factor as seen in Fig. 13 (a). However, it should be noted that only a few grains were investigated in this study. Nevertheless, previous authors have reported that high Schmid factor may not necessarily imply high crack growth rate [28,46]. This is because the Schmid factors were evaluated based on the macroscopic load with the assumption that each grain is under uniform uniaxial stress state. However, stress heterogeneity is induced because of the elastic anisotropy of α grains and the influence of the crack on the local stress field. It should be noted that the underlying phases i.e., α and α + β and the different grain orientations strongly influence the fracture morphology and the level of deformation at the crack front (described using the CTOD parameter) which in turn determines the degree of RICC and PICC. Therefore, exploring the dependency of crack propagation rate on these factors may further explain the acceleration or deceleration of the crack.

The significant role of RICC and PICC in increasing the resistance to the crack propagation when the Schmid factor is relatively high is demonstrated in Fig. 13 (b) and (c). This is especially pronounced at normalized RICC and PICC of above 0.6 and 0.4 which correspond to closure load level of equal to or more than 30% and 50%, respectively. Here, the area of the surface response curve with low crack growth rates i.e., normalized values of below 0.5 increases. In general, an increase in RICC and PICC with a decrease in the Schmid factor leads to low crack growth rates as seen in Fig. 13 (b) and (c), respectively. However, the dependency of crack growth rate on RICC and PICC is limited to the region where the normalized Schmid factor lies below 0.5 which corresponds to the Schmid factor of 0.47. Above a Schmid factor of 0.47, the crack growth rate becomes insensitive to changes in crack closure i.e., the response surface curve is flat implying the stronger effects of high Schmid factor. Interestingly, for the relationship between PICC and Schmid factor with the crack growth rate in Fig. 13 (c), the optimum point occurs at a normalized PICC of 0.7 and not at the maximum value of 1. Since the 3D response surface curve is a rough approximation of the multi-dimensional output from the surrogate model (7D in the current analysis), the shift of the optimum point may result from the fact that other design parameters which influence crack growth rate are kept constant during the generation of the 3D response surface curves. For instance, the optimum point in Fig. 13 (c) which corresponds to the points with the lowest crack growth rates were located on the crack segment which was locally deflected in the interior of α grain (G10) very close to the crack front as highlighted in Fig. 6 (b). This deviation within α grain is associated with the fact that prismatic slip can occur on three independent planes in a single crystal. The measured CTOD along the crack front of this deviated crack segment was mainly below 0.3 μm as observed between 28 and 40 μm along the crack front in Fig. 11. These factors possibly reduced the mode I crack driving force in turn slowing down crack growth.

Indeed, the increase in crack growth rate resistance with increase in crack deflection angle and decrease in CTOD is evident in Fig. 13 (d). However, it should be noted that the short crack propagation rate becomes insensitive to changes in crack deflection angle of below 38° and CTOD of above 0.4 μm i.e., the response surface curve is flat. The slight increase in crack growth at higher deflection angle and low CTOD as seen in Fig. 13 (d) was caused by crack overlap in this region which exhibited large crack extension with fatigue cycling (Fig. 6 (a)) which was not considered in the surrogate model. Moreover, as reported in literature, shear-driven Mode II crack growth mechanism can dominate basal cracking in the short crack regime [17,47]. Therefore, crack acceleration at low CTOD in mode I (Fig. 13 (d)) could be due to crack growth being driven by other crack driving forces such as mode II displacements. This is expected for the highly crystallographic short crack with significant level of crack tilt as reported in Fig. 6. It would be interesting to confirm the trends discussed above on a larger experimental dataset. This could be possible through imaging of two or more regions of interest using imaging-type XMT to obtain a larger dataset for analysis.

This study demonstrated the potential for the combination of projection-type XMT and ultra-high-resolution imaging-type XMT

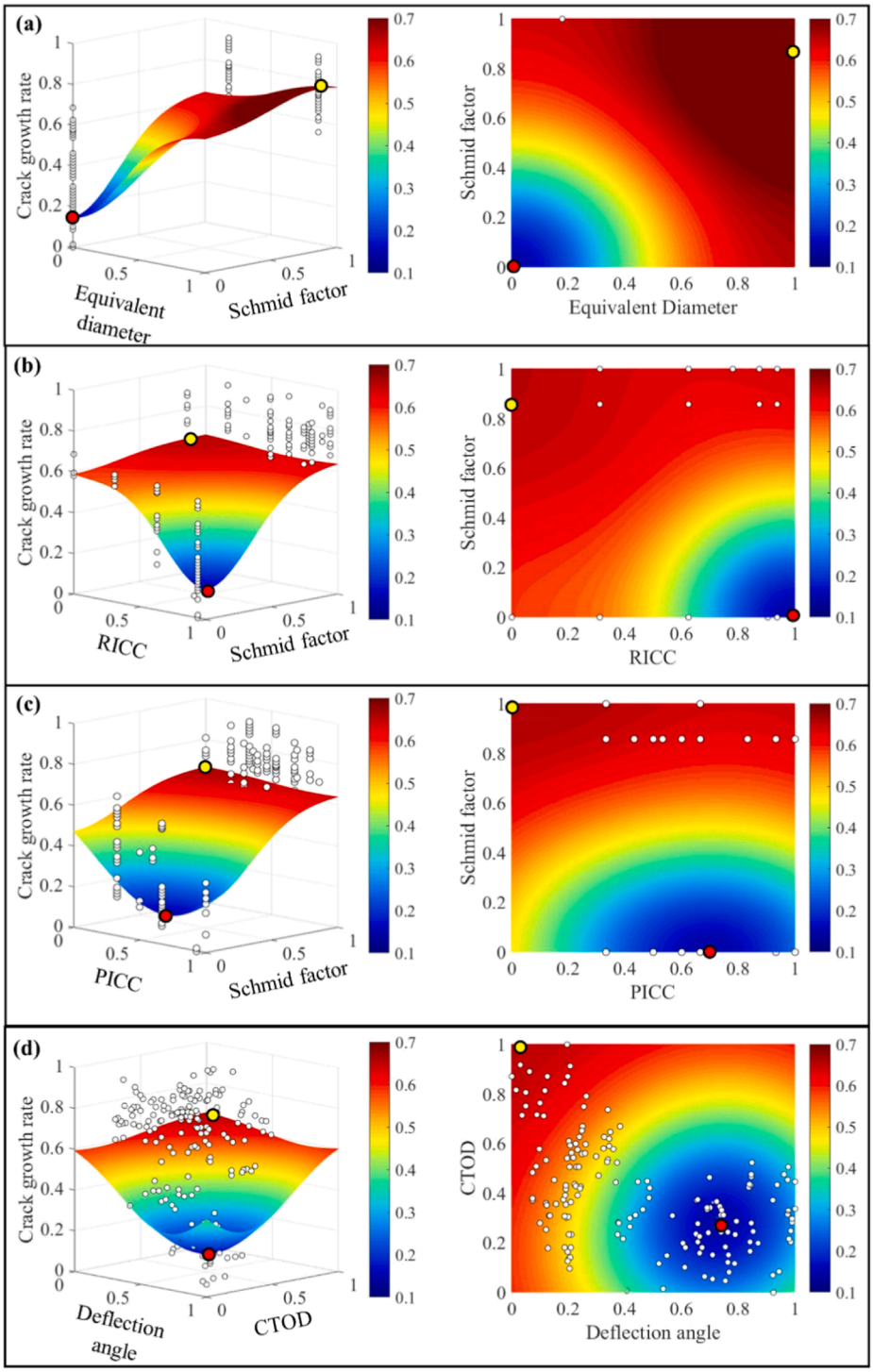

Fig. 13. 3D response surface curves and the projected response curves for equivalent diameter and Schmid factor, RICC and Schmid factor, PICC and Schmid factor, and deflection angle and CTOD with the crack propagation rate in (a), (b), (c), and (d), respectively. In each case the strongest and the weakest point is highlighted by the red and yellow dots, respectively. (For interpretation of the references to color in this figure legend, the reader is referred to the web version of this article.)

techniques for the 3D analysis of short fatigue crack closure and growth behavior over time using a single specimen and in one setting. Using projection-type XMT, the whole gauge section can be imaged to identify areas with phenomenon of interest and the setup can be changed to imaging-type XMT to zoom in to the identified region of interest. It is possible to then superimpose the images acquired using projection-type XMT and imaging-type XMT to see what happens in the region of interest and explain certain localized phenomenon utilizing ultra-high spatial resolution levels. Consequently, this study revealed the importance of ultra-high-resolution imaging-type XMT for the accurate assessment of short fatigue cracks and crack closure especially in high strength materials such as titanium alloys where the crack opening displacement (COD) is very small. The extracted trends using projection XMT from previous studies [6,7,8] which showed strong effect of fracture surface roughness on RICC generation were confirmed in this study using imaging-type XMT. However, at the spatial resolution level of 1 μm,

small features on the fracture surface such as ridges, and local small undulations which are shown to increase incidence of RICC are not captured and can only be visualized using ultra-high-resolution imaging-type XMT. In terms of PICC, by superimposing the same crack segment obtained using projection-type XMT and imaging-type XMT, this study showed that the actual crack front is not captured using projection XMT which implies that PICC cannot be accurately quantified. Therefore, imaging-type XMT technique is invaluable for the analysis of fatigue cracks in materials with low CTOD levels of below 1 μm which is typically seen in high strength materials.

5. Conclusion

The three-dimensional (3D) crack closure behavior of a short fatigue crack in Ti-6Al-4V alloy with a bi-modal microstructure was investigated, in-situ, using ultra-high resolution XMT. Owing to the unprecedented spatial resolution of about 0.15 μm achieved in this study, the intricate 3D fracture morphology with mixed-mode I, II, and III nature was readily visualized. The main findings of this study can be summarized as follows:

1. In 3D, the closure load level varies locally resulting in heterogeneous shielding along the crack front. Through the separation and analysis of roughness-induced and plasticity-induced crack closure, it was elucidated that these mechanisms are controlled by the variation of crack path morphologies which exhibited heterogeneous plastic deformation at the crack tips caused by the anisotropic nature of α grains and varying extents of crack tilting and twisting (i.e., mode II and III displacements) due to the interaction of the crack front with the interface between α and α + β lamellar or the boundary between α grains with different crystallographic orientations.
2. Short crack growth behavior is highly complex and is influenced by the underlying microstructure, the resulting fracture morphology caused by crack front interaction with the local microstructure, and the accompanying crack closure which are highly variable in 3D. Using surrogate-based statistical analysis, the actual dependency of crack growth rate on the above factors was revealed. A general trend of decrease in Schmid factor with decrease in equivalent diameter was found to enhance crack growth resistance. In contrast, beyond certain levels, crack growth rate becomes insensitive to changes in the level of RICC, PICC, deflection angle, and CTOD which are strongly dependent on the underlying microstructure. High RICC and PICC of equal to or more than 30% and 50% closure load level, respectively was found to increase the crack growth resistance when the Schmid factor lies below 0.47. But above the Schmid factor of 0.47, crack growth rate becomes insensitive to changes in crack closure implying the stronger effects of high Schmid factor. It was also revealed that changes in crack deflection angle of below 38° and CTOD of above 0.4 μm does not have any effect on the short crack growth rate which remains high irrespective of the values beyond these limits.

Declaration of Competing Interest

The authors declare that they have no known competing financial interests or personal relationships that could have appeared to influence the work reported in this paper.

Data availability

The raw/processed data required to reproduce these findings cannot be shared at this time as the data also forms part of an ongoing study.

Acknowledgements

The synchrotron radiation experiments were performed at SPring-8 with the approval of JASRI through proposal number 2021A1574. This work was supported through the JSPS Grant-in-aid for Scientific Research, KAKENHI, grant numbers JP21H04624 and JP21H04529, and by JST, CREST Grant Number JPMJCR1995, Japan. One of the authors (Tubei V.) is also grateful for the JSPS Grant-in-aid for Scientific Research, subject number HAG1J12176. The authors would also like to thank Professor Kazuyuki Shimizu from Iwate University who was very instrumental in X-ray tomography data acquisition in SPring-8.

Appendix A. Supplementary data

Supplementary data to this article can be found online at https://doi.org/10.1016/j.ijfatigue.2022.107428.

References

[1] Elber W. The significance of fatigue crack closure. In damage tolerance in aircraft structures, ASTM STP 486. Am Soc Test Mater 1971:232–42.
[2] Paris P, Erdogan F. A critical analysis of crack propagation laws. J Basic Eng 1963; 85:528–33.
[3] Pippan R, Hohenwarter A. Fatigue crack closure: a review of the physical phenomena. Fatigue Fract Eng Mater Struct Apr. 2017;40(4):471–95. https://doi.org/10.1111/ffe.12578.
[4] Birosca S, Buffiere JY, Karadge M, Preuss M. 3-D observations of short fatigue crack interaction with la2mellar and duplex microstructures in a two-phase titanium alloy. Acta Mater Feb. 2011;59(4):1510–22. https://doi.org/10.1016/J.ACTAMAT.2010.11.015.
[5] Schaef W, Marx M, Vehoff H, Heckl A, Randelzhofer P. A 3-D view on the mechanisms of short fatigue cracks interacting with grain boundaries. Acta Mater Mar. 2011;59(5):1849–61. https://doi.org/10.1016/J.ACTAMAT.2010.11.051.
[6] Toda H, et al. A 3D measurement procedure for internal local crack driving forces via synchrotron X-ray microtomography. Acta Mater Mar. 2004;52(5):1305–17. https://doi.org/10.1016/J.ACTAMAT.2003.11.014.
[7] Khor KH, Buffiére JY, Ludwig W, Sinclair I. High resolution X-ray tomography of micromechanisms of fatigue crack closure. Scr Mater 2006;vol. 55, no. 1 SPEC. ISS: 47–50. https://doi.org/10.1016/j.scriptamat.2006.01.016.
[8] Chen R, Zhu M-L, Xuan F-Z, Wu S-C, Fu Y-N. Near-tip strain evolution and crack closure of growing fatigue crack under a single tensile overload. Int J Fatigue May 2020;134:105478. https://doi.org/10.1016/J.IJFATIGUE.2020.105478.
[9] Limodin N, Réthoré J, Buffière J-Y, Hild F, Roux S, Ludwig W, et al. Influence of closure on the 3D propagation of fatigue cracks in a nodular cast iron investigated by X-ray tomography and 3D volume correlation. Acta Mater 2010;58(8):2957–67.
[10] Ravi P, Naragani D, Kenesei P, Park JS, Sangid MD. Direct observations and characterization of crack closure during microstructurally small fatigue crack growth via in-situ high-energy X-ray characterization. Acta Mater 2021;205: 116564. https://doi.org/10.1016/j.actamat.2020.116564.
[11] Tubei V, Toda H, Hassanipour M, Hirayama K, Takakuwa O, Takeuchi A, et al. 3D short fatigue crack closure behavior in Ti-6Al-4V alloy investigated using in-situ high resolution synchrotron X-ray tomography. Eng Fract Mech 2021;249:107755.
[12] Suzuki Y, Toda H. in Advanced tomographic Methods in Material Research and Engineering. Oxford University Press; 2008.
[13] Takeuchi A, Uesugi K, Suzuki Y, Aoki S. Hard X-ray Microtomography Using X-ray Imaging Optics. Japan Soc Appl Phys 2001;40:1499–503.
[14] Liss K-D, Bartels A, Schreyer A, Clemens H. High-Energy X-Rays: A tool for Advanced Bulk Investigations in Materials Science and Physics. Textures Microstruct 2003;35(3–4):219–52. https://doi.org/10.1080/07303300310001634952.
[15] Takeuchi A, Uesugi K, Suzuki Y, Itabashi S, Oda M. Fresnel zone plate with apodized aperture for hard X-ray Gaussian beam optics. J Synchrotron Radiat 2017;24(3):586–94. https://doi.org/10.1107/S1600577517003289.
[16] Bantounas I, Dye D, Lindley TC. The role of microtexture on the faceted fracture morphology in Ti-6Al-4V subjected to high-cycle fatigue. Acta Mater 2010;58(11): 3908–18. https://doi.org/10.1016/j.actamat.2010.03.036.
[17] Hémery S, Stinville JC. Microstructural and load hold effects on small fatigue crack growth in α+β dual phase Ti alloys. Int J Fatigue 2021;156(September):2022. https://doi.org/10.1016/j.ijfatigue.2021.106699.
[18] Shin CS, Smith RA. Fatigue crack growth at stress concentrations-the role of notch plasticity and crack closure. Eng Fract Mech 1988;29(3):301–15. https://doi.org/10.1016/0013-7944(88)90019-7.
[19] Gall K, Sehitoglu H, Kadioglu Y. Plastic zones and fatigue-crack closure under plane-strain double slip. Metall Mater Trans A 1996;27A:3491–502.
[20] Hassanipour M, Watanabe S, Hirayama K, Toda H, Uesugi K, Takeuchi A. Short crack growth behavior and its transitional interaction with 3D microstructure in Ti-6Al-4V. Mater Sci Eng A Dec. 2018;738:229–37. https://doi.org/10.1016/J.MSEA.2018.09.073.
[21] Lavogiez C, Hémery S, Villechaise P. Analysis of deformation mechanisms operating under fatigue and dwell-fatigue loadings in an α/β titanium alloy. Int. J. Fatigue 2020;131(July 2019). https://doi.org/10.1016/j.ijfatigue.2019.105341.
[22] Smith WS. The Scientist and Engineer's Guide to Digital Signal Processing. Second edi: California Technical Publishing; 1999.
[23] Toda H. X-Ray CT: Hardware and Software Techniques. Springer; 2021.

[24] Briffod F, Bleuset A, Shiraiwa T, Enoki M. Effect of crystallographic orientation and geometrical compatibility on fatigue crack initiation and propagation in rolled Ti-6Al-4V alloy. Acta Mater 2019;177:56–67. https://doi.org/10.1016/j.actamat.2019.07.025.
[25] Hassanipour M, Watanabe S, Hirayama K, Toda H, Uesugi K, Takeuchi A. Effects of 3D microstructural distribution on short crack growth behavior in two bimodal Ti–6Al–4V alloys. Mater Sci Eng A Oct. 2019;766:138264. https://doi.org/10.1016/J.MSEA.2019.138264.
[26] Ludwig W, Buffière J-Y, Savelli S, Cloetens P. Study of the interaction of a short fatigue crack with grain boundaries in a cast Al alloy using X-ray microtomography. Acta Mater Feb. 2003;51(3):585–98. https://doi.org/10.1016/S1359-6454(02)00320-8.
[27] Zhai T, Wilkinson AJ, Martin JW. A crystallographic mechanism for fatigue crack propagation through grain boundaries. Acta Mater Dec. 2000;48(20):4917–27. https://doi.org/10.1016/S1359-6454(00)00214-7.
[28] Herbig M, King A, Reischig P, Proudhon H, Lauridsen EM, Marrow J, et al. 3-D growth of a short fatigue crack within a polycrystalline microstructure studied using combined diffraction and phase-contrast X-ray tomography. Acta Mater 2011;59(2):590–601.
[29] Limodin N, Réthoré J, Buffière J-Y, Gravouil A, Hild F, Roux S. Crack closure and stress intensity factor measurements in nodular graphite cast iron using three-dimensional correlation of laboratory X-ray microtomography images. Acta Mater Aug. 2009;57(14):4090–101. https://doi.org/10.1016/J.ACTAMAT.2009.05.005.
[30] Hémery S, Nizou P, Villechaise P. In situ SEM investigation of slip transfer in Ti-6Al-4V: Effect of applied stress. Mater Sci Eng A 2018;709(August 2017):277–84. https://doi.org/10.1016/j.msea.2017.10.058.
[31] Song JH, Chung YI. A review of crack closure measurement by compliance technique and the normalized-extended ASTM method as a currently most refined, practical and simple one. Procedia Eng 2010;2(1):777–86. https://doi.org/10.1016/j.proeng.2010.03.084.
[32] Dunne FPE, Rugg D, Walker A. Lengthscale-dependent, elastically anisotropic, physically-based hcp crystal plasticity: Application to cold-dwell fatigue in Ti alloys. Int J Plast 2007;23(6):1061–83. https://doi.org/10.1016/j.ijplas.2006.10.013.
[33] Bantounas I, Lindley TC, Rugg D, Dye D. Effect of microtexture on fatigue cracking in Ti–6Al–4V. Acta Mater Sep. 2007;55(16):5655–65. https://doi.org/10.1016/J.ACTAMAT.2007.06.034.
[34] Queipo NV, Haftka RT, Shyy W, Goel T, Vaidyanathan R, Kevin Tucker P. Surrogate-based analysis and optimization. Prog Aerosp Sci 2005;41(1):1–28. https://doi.org/10.1016/j.paerosci.2005.02.001.
[35] Hassanipour M, Watanabe S, Hirayama K, Li H, Toda H, Uesugi K, et al. Assessment of predominant microstructural features controlling 3D short crack growth behavior via a surrogate approach in Ti-6Al-4V. Mater Sci Eng A 2019;751:351–62.
[36] Liu R, Kumar A, Chen Z, Agrawal A, Sundararaghavan V, Choudhary A. A predictive machine learning approach for microstructure optimization and materials design. Sci Rep 2015;5:1–12. https://doi.org/10.1038/srep11551.
[37] Li H, Gutierrez L, Toda H, Kuwazuru O, Liu W, Hangai Y, et al. Identification of material properties using nanoindentation and surrogate modeling. Int J Solids Struct 2016;81:151–9.
[38] Jollife IT, Cadima J. Principal component analysis: A review and recent developments. Philos Trans R Soc A Math Phys Eng Sci 2016;374(2065):pp. https://doi.org/10.1098/rsta.2015.0202.
[39] Saltelli A, Ratto M, Andres T, Campolongo F, Cariboni J, Gatelli D, Saisana M, Tarantola S, editors. Global Sensitivity Analysis. The Primer. Wiley; 2007.
[40] Taylor R. Interpration of the correlation coefficient: A basic review. J Diagnostic Med Sonogr 1990:35–9.
[41] Cortes C, Vapnik V. Support-Vector Networks. Mach Learn 1995;20(3):273–97.
[42] Khuri AI, Mukhopadhyay S. Response surface methodology. Wiley Interdiscip Rev Comput Stat 2010;2(2):128–49. https://doi.org/10.1002/wics.73.
[43] Toda H, et al. "Surrogate-based optimization for 3D image-based simulation acceleration for structural materials. Acta Mater 2022 [Manuscript in preparation]",.
[44] Przybyla CP, McDowell DL. Microstructure-sensitive extreme-value probabilities of high-cycle fatigue for surface vs. subsurface crack formation in duplex Ti-6Al-4V. Acta Mater 2012;60(1):293–305. https://doi.org/10.1016/j.actamat.2011.09.031.
[45] Tokaji K, Ogawa T, Ohya K. The effect of grain size on small fatigue crack growth in pure titanium. Int J Fatigue Jan. 1994;16(8):571–8. https://doi.org/10.1016/0142-1123(94)90483-9.
[46] Proudhon H, Li J, Ludwig W, Roos A, Forest S. Simulation of Short Fatigue Crack Propagation in a 3D Experimental Microstructure. Adv Eng Mater 2017;19(8):1–9. https://doi.org/10.1002/adem.201600721.
[47] Maenosono A, Koyama M, Tanaka Y, Ri S, Wang Q, Noguchi H. Crystallographic selection rule for the propagation mode of microstructurally small fatigue crack in a laminated Ti-6Al-4V alloy: Roles of basal and pyramidal slips. Int J Fatigue Nov. 2019;128:105200. https://doi.org/10.1016/J.IJFATIGUE.2019.105200.